DOI: 10.1002/anie.201303740

Nanoparticles

Electron-Beam-Induced Deposition of Bimetallic Nanostructures from Bulk Liquids**

Matthew Bresin, Adam Chamberlain, Eugenii U. Donev, Chandan B. Samantaray, Gregory S. Schardien, and J. Todd Hastings*

The fields of electron-beam-induced deposition (EBID) and pulse radiolysis have long been known to share a commonality where energetic particles, impinging on (or traversing though) condensed matter, cause chemical reactions in precursors. Further comparisons between these two techniques have been hampered as pulse radiolysis employs liquid-phase precursors, while EBID precursors are typically gases. Using a hybrid technique known as liquid-phase electron-beam-induced deposition (LP-EBID) we have investigated the application of well-known pulse radiolysis chemical kinetics to the LP-EBID process. We report that bimetallic deposits (AuAg and AuPt) produced with LP-EBID follow chemical kinetics found in pulse radiolysis studies, leading to predictable compositions. In addition, TEM results show the deposits are alloyed, consistent with high dose pulse radiolysis for similar materials.

While previous results in LP-EBID have shown the successful deposition of metal nanostructures with high purity,[1–3] the chemical mechanism itself has received limited attention. It is likely that the mechanism shares similarities with both gas-phase EBID and pulse radiolysis. For instance, in pulse radiolysis,[4] aqueous solutions containing metal ion complexes are exposed to high-energy electrons, ions, or photons with megaelectron volt energy, resulting in suspended or otherwise randomly distributed nanoparticles over a large irradiated area. In EBID[5,6] the electron source is a relatively low-energy (keV) electron beam from a scanning electron microscope (SEM), allowing for site-specific patterning of nanoscale structures.

While the methodologies for producing nanoscale structures differ, both techniques are thought to induce chemical reactions through the generation of secondary species, such as the solvated electron in pulse radiolysis and secondary electrons in EBID. Solvated electrons are well-known to act as reducing agents for the generation of metal clusters[7,8] and to cause damage in biological specimens such as DNA.[9] Similarly, secondary electrons with energies between 0–20 eV have been shown to bind to gas-phase EBID precursors, such as $Pt(PF_3)_4$[10] and $Co(CO)_3NO$[11] leading to molecular dissociation.

Since both pulse radiolysis and EBID have known mechanisms with secondary species, we hypothesize that similar mechanisms would be present in LP-EBID. As LP-EBID precursor solutions typically contain micro- to millimolar concentrations of ionic complexes, it is likely that primary electrons will react with H_2O molecules to produce various radicals, including solvated electrons, rather than reacting directly with the ionic complexes. Indeed, here we demonstrate that established rate constants of reactions between solvated electrons and metal ions can be applied to the resulting LP-EBID nanostructures, resulting in an excellent fit to multiple precursor concentrations for both AuAg and AuPt. These results show that LP-EBID bears a strong similarity to pulse radiolysis, and furthermore that extant literature can be applied to the site-specific deposition of high-purity materials.

In contrast to gas-phase EBID, liquid-phase experiments are most easily conducted on polyimide or silicon nitride membranes that serve to separate the solution from the vacuum of the electron-beam lithography system as illustrated in Figure 1a. The electron beam energy is sufficient to penetrate the polyimide window and subsequently induce ion–electron reactions in the liquid reservoir. As depicted in the inset of Figure 1a, deposition occurs on the liquid side of the polyimide window in proximity to the primary beam (additional details in the Supporting Information). Once the deposition process is complete, the top portion of the cell can be extracted for ex situ imaging. Figure 1b–e show top-down dark-field scanning transmission electron microscope images of AuAg and AuPt deposits recorded by scanning electron microscopy (Quanta FEG, FEI, Hillsboro, OR USA). Figure 1b and d demonstrate the site-specific deposition capabilities of LP-EBID, whereas Figures 1c and e show the cluster or colloidal aspects of the deposits. For both AuAg and AuPt, the primary dot pattern is surrounded by varying levels of unintended, or collateral, deposition (additional discussion regarding the deposit morphology can be found in the Supporting Information). Figure 2a shows nanoscale dots deposited from solutions containing varying concentrations of $HAuCl_4$ and H_2PtCl_6 acids. Figure 2b shows similar results for mixtures of $HAuCl_4$ and $AgNO_3$. The deposits in Figure 2a

---

[*] Dr. M. Bresin, A. Chamberlain, Dr. E. U. Donev, Dr. C. B. Samantaray, G. S. Schardien, Prof. Dr. J. T. Hastings
Department of Electrical and Computer Engineering
University of Kentucky
453 F. Paul Anderson Tower, Lexington, KY (USA)
E-mail: hastings@engr.uky.edu

[**] This material is partially based upon work supported by the Defense Advanced Research Projects Agency (DARPA) under award number N66001-09-1-2099. This material is also based upon work supported by the National Science Foundation under grant number CMMI-1125998. The authors thank C. May, B. Wajdyk, and the University of Kentucky Center for Nanoscale Science and Engineering as well as J. Ye, L. Rice, and the University of Kentucky Electron Microscopy Center for valuable technical support.

Supporting information for this article is available on the WWW under http://dx.doi.org/10.1002/anie.201303740.

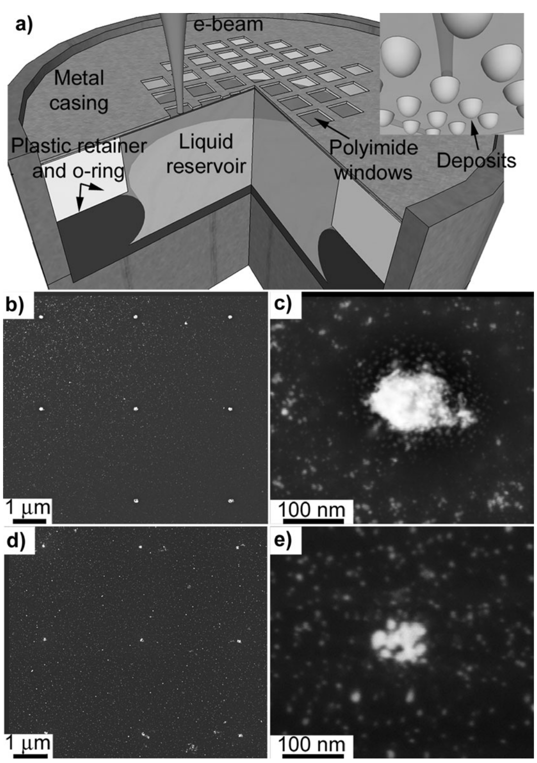

Figure 1. The liquid cell and examples of deposited patterns. a) Liquid precursors are contained within the sealed capsule and are accessible through an electron transparent polyimide membrane. Inset: The electron beam penetrates the thin polyimide membrane, inducing deposition on the liquid side. b) Ex situ (liquid side) dark-field scanning transmission electron micrograph (DF-STEM) of AuAg deposits produced with a dot dose of 60 pC. c) High-resolution image of an ex situ (liquid side) single deposit, showing partially imbedded colloidal AuAg particles. d) DF-STEM of AuPt deposits produced with a dot dose of 10 pC. e) High-resolution image of a colloidal AuPt deposit.

and b illustrate that arrayed nanoscale features are attainable at each solution concentration studied.

Perhaps the most intriguing aspect of this work is the clear relationship between deposit composition and solution composition. Figure 2c and d plot the fraction of the primary elements in the deposits (AuPt and AuAg, respectively) versus the concentration of the ion complexes in solution from Figure 2a and b. Values for the primary element composition are obtained from energy-dispersive X-ray (EDX) spectra, where the metal content fractions are simulated using the NIST DTSA-II software. Example fitting is shown in Figure 2e and f. Relative rate curves were produced by taking the limiting reaction rate and concentration ratio, $k_{\mathrm{M1}}C_{\mathrm{M1}}/(k_{\mathrm{M2}}C_{\mathrm{M2}})$. The predicted concentrations are based on the rate constant of the first reaction step between $[\mathrm{AuCl_4}^-]$ or $[\mathrm{PtCl_6}^{2-}]$ and a solvated electron, e^-(aq.), and do not contain any fitting parameters.

The overall reactions for Au and Pt, omitting several intermediate steps, and the measured rate constants for the first step taken from Ref. [8] are given in Equations (1) and (2).

$$[\mathrm{AuCl_4}]^- + e_{\mathrm{aq}}{}^- \rightarrow \mathrm{Au}^0 \qquad k = 6.1\times10^{10}\ \mathrm{M}^{-1}\,\mathrm{s}^{-1} \tag{1}$$

$$[\mathrm{PtCl_6}]^{-2} + e_{\mathrm{aq}}{}^- \rightarrow \mathrm{Pt}^0 \qquad k = 1.9\times10^{10}\ \mathrm{M}^{-1}\,\mathrm{s}^{-1} \tag{2}$$

The excellent match between the predicted and experimental atomic fractions suggests that the first reaction step is rate-limiting for both elements.

Figure 2d shows a similar map between solution and deposit concentration for AuAg structures. In this case three reaction steps are required to produce stable metallic silver. In all cases we assume the precursor ion concentration, $[\mathrm{Ag}^+]$, far exceeds that of the other reactants.

The first two reaction steps are given in Equations (3) and (4),[12]

$$\mathrm{Ag}^+ + e_{\mathrm{aq}}{}^- \rightarrow \mathrm{Ag}^0 \qquad k = 4.8\times10^{10}\ \mathrm{M}^{-1}\,\mathrm{s}^{-1} \tag{3}$$

$$\mathrm{Ag}^+ + \mathrm{Ag}^0 \rightarrow \mathrm{Ag_2}^+ \qquad k = 8.5\times10^{9}\ \mathrm{M}^{-1}\,\mathrm{s}^{-1} \tag{4}$$

and the reaction is completed by Equation (5).[13]

$$\mathrm{Ag_2}^+ + \mathrm{Ag}^+ \rightarrow \mathrm{Ag}^{+2} + \mathrm{Ag_2} \tag{5}$$

The rate constant of the first step is far faster than the second, and thus does not accurately predict the deposit composition. However, the rate constant for the second reaction step provides an excellent match to the experimental data, and appears to be the rate-limiting step.

These results are particularly exciting because they suggest that one may be able to identify rate-limiting reaction steps from available pulse radiolysis data and then predict the deposit composition for bimetallic electron-beam-induced deposition.

The deposit compositions were analyzed by EDX spectroscopy, and found to contain a combined metal composition typically exceeding 90 at.%. The primary contaminant for the AuPt structures is Cl, with a content of 9.4 ± 0.9 at.%. The contamination is presumably a result of byproducts from the chloroaurate and chloroplatinate ions. This is consistent with previous work on Au and Pt deposited separately.[1,2] Likewise, the primary discernible contaminant in AuAg structures is also Cl with a content of 5.6 ± 0.8 at.%, again from $[\mathrm{AuCl_4}]^-$. Oxygen, carbon, and nitrogen could conceivably be incorporated in the deposits from the environment; however, as these elements are present in the membrane, their respective concentrations in the deposit are difficult to assess.

In addition, we investigated the effects of dose on the composition. For example, reagents with faster reaction rates could conceivably be locally depleted at long deposition times (high dose) because of mass transport limitations. To test this possibility we acquired EDX spectra from 11 nanoparticles of 1:1 AuPt deposits exposed with doses between 12 and 132 pC (pC = picocoulomb). Variation in the Au:Pt ratio for these deposits is ±3 at.%, which is within the error of the EDX measurement. Moreover, the maximum and minimum Pt concentrations occur at 108 and 48 pC, respectively, as opposed to the extremes of the dose range. Thus, over a practical dose range and within experimental error, we have not been able to discern a relationship between dose and deposit composition.

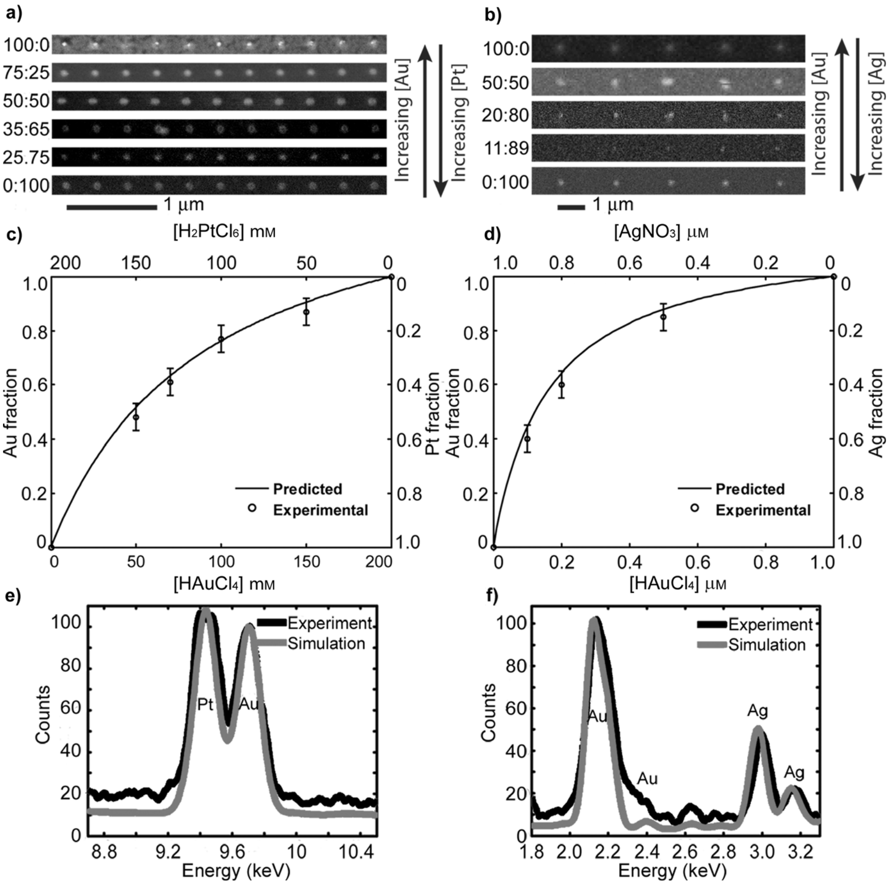

Figure 2. Predicted versus experimental composition of bimetallic deposits. a) AuPt patterns deposited from solutions of $HAuCl_4$ and H_2PtCl_6 with a total concentration of 200 μM and a dot dose of 100 pC. The solution concentration ratios are listed next to each set of deposits. b) AuAg patterns deposited from solutions of $HAuCl_4$ and $AgNO_3$ with a total concentration of 1 mM and a dot dose of 100 pC. c) Experimental data and relative rate curve [Eqs. (1) and (2)] for AuPt deposits. No fitting parameters are used in the predicted models. d) Experimental data and relative rate curve [Eqs. (1) and (4)] for AuAg deposits. e) Example EDX spectrum from a bimetallic AuPt deposit. The experimental data is well-matched by the simulated spectrum with a 50:50 Au:Pt ratio. The Au:Pt ratio in solution was 25:75. f) Example EDX spectrum from a bimetallic AuAg deposit. The experimental data is well-matched by the simulated spectrum with a 40:60 Au:Ag ratio. The Au:Ag ratio in solution was 10:90.

Treguer et al. have shown that pulse radiolysis of solutions containing Ag^+ and $AuCl_4^-$ yielded either bilayer or alloy nanoparticles at lower ($35\,kGy\,h^{-1}$) and higher ($7.9\times 10^3\,kGy\,h^{-1}$) dose rates, respectively.[7] At low-dose rates the silver atoms act as an electron relay for gold atoms, leading to the formation of gold core–silver shell particles. At high-dose rates, both Ag and Au atoms are fully reduced before subsequent electron transfer can occur, leading to alloy particles. We can place a conservative lower bound on the dose rate for our experiments by assuming that all of the primary electron energy is dissipated in a spherical volume with a diameter equal to the Bethe range of 20 keV electrons in water (see the Supporting Information for discussion). This yields a dose rate of approximately $2\times 10^7\,kGy\,h^{-1}$. At these high-dose rates one would expect only alloy formation, which is consistent with TEM observations of the bimetallic deposits (micrographs and additional information are available in the Supporting Information).

Bimetallic nanostructures are deposited here by simply mixing liquid precursors, where deposit composition can be predicted using established rate constants of reactions between solvated electrons and metal ions. In contrast, there are few examples of multi-element material deposition exist using EBID (with the recent exceptions of CoPt[14] and PtSi[15] deposition), because of the complexities in controlling injection, adsorption, and dissociation of multiple gas-phase precursors. In addition, the techniques and solutions described here are applicable to direct observation of crystal growth[16] and liquid-phase imaging,[17] while the nanostructures may have applications in fields such as patterned catalysis.[18]

In conclusion, electron-beam-induced deposition from bulk liquids appears promising for patterning bimetallic nanostructures. Moreover, bimetallic structures appear to follow their single-element counterparts in terms of low-contamination levels. At experimentally preferable precursor concentrations and deposition doses, the deposit composition appears to be dose-independent within our current measurement capabilities. Finally, and most importantly, rate constants established over many years using pulsed radiolysis to study solvated electron–metal ion reactions can prove predictive of bimetallic deposit composition. These findings indicate that a more substantial intellectual bridge should be built between the long-standing field of radiation chemistry and the emergent area of electron-beam-induced processing.

Experimental Section

All deposition processes were conducted in a Raith e-LiNE electron beam lithography (EBL) system using a 20 keV electron beam and a beam current of 1.3 nA. Depositions were carried out on 150 nm thick polyimide membranes that form the top of commercial liquid electron-microscopy capsules (Quantomix, QX-102 WETSEM). The liquid cells contained 15 μL of precursor solution. Colloidal gold nanoparticles (about 50 nm in diameter) were placed on the vacuum side of the membrane to aid in focusing, while patterns were created on the bottom side of the membrane in contact with the precursor liquid. AuPt dots were patterned in arrays with doses ranging from 100–1100 pC per dot with periods of 350 nm. AuAg dots were patterned in arrays with doses ranging from 50–150 pC per dot with periods of 2 μm. Finally, all the samples were rinsed with deionized water for several minutes and dried in air once they were removed from the EBL chamber. Elemental analysis was conducted with energy-dispersive X-ray spectroscopy (Evex Si(Li)) in a Hitachi S-3200 SEM using a 20 keV primary beam and confirmed for one AuAg and one AuPt deposit in a JEOL-2010f TEM (Oxford Si(Li)) using a 200 keV primary beam. Monte Carlo simulation-based analysis using in NIST DTSA-II software package was used to quantify the deposit compositions. Error bounds on the deposit compositions were established by using a simulated 1:1 AuAg film as a baseline and taking the largest compositional deviation among simulations of 10 and 100 nm thick films both with and without infinite polyimide substrates. The resulting 10% relative error is consistent with conventional interpretation of standardless EDX analysis.

The precursor solutions were prepared in deionized water (18 MΩ) from H_2PtCl_6, $HAuCl_4$, and $AgNO_3$. All chemicals were obtained from Sigma–Aldrich and used as received. For the AuPt nanostructures total solute concentrations were fixed at 200 μM while the individual precursor concentrations were varied between pure $HAuCl_4$ and pure H_2PtCl_6 as Au (200 μM), Au (150 μM) + Pt (50 μM), Au (100 μM) + Pt (100 μM), Au (70 μM) + Pt (130 μM), Au (50 μM) + Pt (150 μM), and Pt (200 μM). For the AuAg nanostructures the total solute concentration was fixed at 1 mM while the individual precursor concentrations varied between pure $HAuCl_4$ and pure $AgNO_3$ as Au (1.0 mM), Au(0.50 mM) + Ag (0.50 mM), Au (0.20 mM) + Ag (0.80 mM), Au(0.11 mM) + Ag (0.89 mM), and Ag (1.0 mM).

Received: May 2, 2013

Keywords: bimetallic nanostructures · electron-beam-induced deposition · nanoparticles · solvated electrons

---

[1] G. Schardein, E. U. Donev, J. T. Hastings, *Nanotechnology* **2011**, *22*, 015301.
[2] E. U. Donev, J. T. Hastings, *Nano Lett.* **2009**, *9*, 2715 – 2718.
[3] L. E. Ocola, A. Joshi-Imre, C. Kessel, B. Chen, J. Park, D. Gosztola, R. Divan, *J. Vac. Sci. Technol. B* **2012**, *30*, 06FF08-07.
[4] G. V. Buxton, Q. G. Mulazzani, A. B. Ross, *J. Phys. Chem.* **1995**, *24*, 1055 – 1349.
[5] I. Utke, P. Hoffmann, J. Melngailis, *J. Vac. Sci. Technol. B* **2008**, *26*, 1197 – 1276.
[6] I. Utke, A. Gölzhäuser, *Angew. Chem.* **2010**, *122*, 9516 – 9518; *Angew. Chem. Int. Ed.* **2010**, *49*, 9328 – 9330.
[7] M. Treguer, C. de Cointet, H. Remita, J. Khatouri, M. Mostafavi, J. Amblard, J. Belloni, R. de Keyzer, *J. Phys. Chem. B* **1998**, *102*, 4310 – 4321.
[8] D. Behar, J. Rabani, *J. Phys. Chem. B* **2006**, *110*, 8750 – 8755.
[9] E. Alizadeh, L. Sanche, *Chem. Rev.* **2012**, *112*, 5578 – 5602.
[10] J. F. Friedman, T. M. Miller, J. K. Friedman-Schaffer, A. A. Viggiano, G. K. Rekha, A. E. Stevens, *J. Chem. Phys.* **2008**, *128*, 104303 – 104306.
[11] S. Engmann, M. Stano, Š. Matejčík, O. Ingólfsson, *Angew. Chem.* **2011**, *123*, 9647 – 9649; *Angew. Chem. Int. Ed.* **2011**, *50*, 9475 – 9477.
[12] E. Janata, A. Henglein, B. G. Ershov, *J. Phys. Chem.* **1994**, *98*, 10888 – 10890.
[13] E. J. Hart, M. Anbar, *The hydrated electron*, Wiley-Interscience, New York, NY, **1970**, p. 122, and references therein.
[14] F. Porrati, E. Begun, M. Winhold, H. S. Ch, R. Sachser, A. S. Frangakis, M. Huth, *Nanotechnology* **2012**, *23*, 185702.
[15] M. Winhold, C. H. Schwalb, F. Porrati, R. Sachser, A. S. Frangakis, B. Kämpken, A. Terfort, N. Auner, M. Huth, *ACS Nano* **2011**, *5*, 9675 – 9681.
[16] J. M. Yuk, J. Park, P. Ercius, K. Kim, D. J. Hellebusch, M. F. Crommie, J. Y. Lee, A. Zettl, A. P. Alivisatos, *Science* **2012**, *336*, 61 – 64.
[17] N. de Jonge, F. M. Ross, *Nat. Nanotechnol.* **2011**, *6*, 695 – 704.
[18] J.-U. Park, S. Nam, M.-S. Lee, C. M. Lieber, *Nat. Mater.* **2012**, *11*, 120 – 125.